FRACTURE RESPONSE OF EXTERNALLY FLAWED CYLINDRICAL SHELLS TO INTERNAL GASEOUS DETONATION LOADING

Tong Wa Chao and **Joseph E. Shepherd**
California Institute of Technology
Graduate Aeronautical Laboratories
Pasadena, CA 91125
U.S.A.

Abstract

Experiments were performed to observe the fracture behavior of thin-wall and initially-flawed aluminum tubes to internal gaseous detonation loading. The pressure load, with speeds exceeding 2 km/s, can be characterized as a pressure peak (ranging from 2 to 6 MPa in these experiments) followed by an expansion wave. Flaws were machined as external axial surface notches. Cracks ran both in the upstream and downstream directions as the hoop stress opened up the notch. Different kinds of crack propagation behavior were observed for various loading amplitudes and flaw sizes. For low-amplitude loading and short flaws, cracks tend to run in a helical fashion, whereas for high-amplitude loading and long flaws, cracks tend to bifurcate in addition to running helically. Unless the cracks branched and traveled far enough to meet, resulting in a split tube, they were always arrested. Strain gages were used to monitor the hoop strains at several places on the tubes' external surface. Far away from the notch, tensile vibrations were measured with frequencies matching those predicted by the steady-state Tang (1965) and Simkins (1987) models. Near the notch, compressive strains were recorded as a result of the bulging at the notch. Features in the strain signals corresponding to different fracture events are analyzed.

Nomenclature

E	Young's modulus	$\mathrm{N/m^2}$
G	shear modulus	$\mathrm{N/m^2}$
R	shell mean radius	m
h	shell thickness	m
l	shell length	m
P_{cj}	Chapman-Jouguet pressure	Pa
U_{cj}	Chapman-Jouguet velocity	m/s
v	shock speed	m/s
v_d	dilatational wave speed	m/s
β	shell thickness parameter	
Δp	pressure difference across shell	Pa
κ	shear correction factor	
ν	Poisson's ratio	
ρ	density	$\mathrm{kg/m^3}$
K_{Ic}	Mode-I fracture toughness	$\mathrm{MPa}\sqrt{\mathrm{m}}$
σ	stress	$\mathrm{N/m^2}$
d	initial notch depth	m
$2a$	initial notch length (model)	m
L	initial notch length (experiment)	m

1 Introduction

This study is motivated by the fracture mechanics driven design and safety criteria for pulse detonation engines and gaseous detonation tubes. The usual design strategy is to minimize stress concentrations to prevent cracks from initiating. If cracks do initiate, the goal of fracture-based design is to prevent catastrophic failure by bringing the cracks to quick and benign arrest. Fracture mechanics analysis requires the presence of an initial flaw in the structure. Crack initiation, propagation, and arrest are then governed by loading, geometry, and material properties.

Although literature on fracture mechanics of pressure vessels and pipelines is abundant, most of it deals with quasi-static (e.g., Folias (1965), Maxey et al. (1971), or Kiefner

et al. (1973)) or fatigue loading. The structural response of shells to shock or detonation loading was studied by researchers such as Tang (1965), Reismann (1965), de Malherbe et al. (1966), and Simkins (1987), but these were done on unflawed tubes and therefore did not involve a fracture mechanics approach. This study attempts to bridge fracture mechanics and cylindrical shell dynamics.

The experiments here concern two aspects. The first is the qualitative behavior of the crack path of a fractured tube as a function of initial flaw length. The second deals with the quantitative measurements of strain history on the rupturing tube, and an attempt to estimate a fracture threshold. The fracture threshold divides a non-dimensional parametrized test space into rupture (i.e., surface notch becoming a through-wall crack) and no rupture zones. Given a detonation wave of certain magnitude and a flaw of certain size, one can use this threshold model to estimate whether a surface flaw will break through the wall.

Previous work was done at Caltech by Beltman et al. (1999) and Beltman and Shepherd (2002) to investigate the structural response of unflawed cylindrical shells to internal shock and detonation loading. These analytical, numerical, and experimental studies demonstrated that the amplitude of the linear elastic strains are related to the speed of the shock or detonation wave. The present work extends this to the structural failure regime.

2 Analytical models

The analytical models in this section consist of one that predicts dynamic strains due to flexural wave excitation in unflawed cylindrical shells, and another one that predicts the stress intensity factor based on the static model of a surface-cracked plate.

2.1 Unflawed Tubes and the Dynamic Amplification Factor

The model presented by Tang (1965) enables the calculation of the steady-state linearly elastic strains (in the shock-fixed frame) of an unflawed thin wall tube subjected to shock or detonation loading. The formulation includes shear deformation and rotary inertia. The model implies that there are four critical speeds associated with the structural waves excited by the traveling pressure load. The speed v_{c0} is the first critical velocity and corresponds to a resonance between the group velocity of the structural waves and the phase velocity of the detonation (see the extensive discussion in Beltman and Shepherd (2002)). The values of each critical velocity can be calculated from the vanishing of the discriminant

$$A_2^2 - 4A_0A_4 = 0 \,, \tag{1}$$

where

$$\begin{aligned} A_4 &= \left[\left(\frac{v}{v_d}\right)^2 - 1\right]\left[\left(\frac{v}{v_s}\right)^2 - 1\right] \,, \\ A_2 &= \left(\frac{v}{v_d}\right)^2\left[1+\beta^2\left(\frac{v_d}{v_s}\right)^2\right] - \beta^2\left(1-\nu^2\right)\left(\frac{v_d}{v_s}\right)^2 \,, \\ A_0 &= \beta^2 + \frac{\beta^2\nu^2}{\left[\left(\frac{v}{v_d}\right)^2 - 1\right]} \,, \end{aligned} \tag{2}$$

where the shell thickness parameter is

$$\beta = \frac{h}{\sqrt{12}R} \,. \tag{3}$$

The other critical velocities are v_{c1}, equal to the shear wave speed v_s

$$v_s = \sqrt{\frac{\kappa G}{\rho}} \,; \tag{4}$$

v_{c2}, equal to the dilatational wave speed in a bar $v_d\sqrt{1-\nu^2}$, and v_{c3}, equal to the dilatational wave speed v_d

$$v_d = \sqrt{\frac{E}{\rho\left(1-\nu^2\right)}} \,. \tag{5}$$

For a more detailed discussion on these cases, the reader is referred to Tang (1965).

The dynamic amplification factor is defined as the ratio between the maximum dynamic strain and the equivalent static strain calculated from static formulas using the measured peak applied pressure

$$\Phi = \frac{\epsilon_{dynamic\_max}}{\epsilon_{static}} \tag{6}$$

and is plotted as a function of the detonation or shock wave speed in Fig. 1. This factor goes from about 1 below v_{c0} to unbounded at v_{c0}, and drops to about 2 between v_{c0} and v_{c1}. Since the present experiments operate at the region far above v_{c0} but below v_{c1}, the dynamic amplification factor can be approximated as 2.

2.2 Flawed Tubes and the Fracture Threshold

In linear elastic fracture mechanics, mode-I fracture initiates when the stress intensity factor K_I reaches the fracture toughness K_{Ic}. Since currently there is no analytical model for the dynamic stress intensity factor for a detonation tube with an external axial flaw, static relations will be used to infer the stress intensity factor. A dynamic amplification

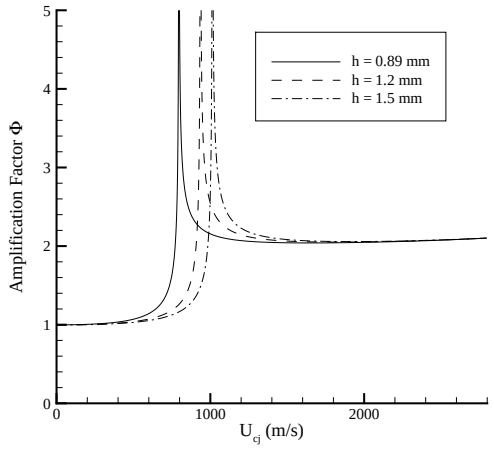

Figure 1: Steady-state dynamic amplification factor as a function of detonation wave speed according to the Tang (1965) model. Curves for Al6061-T6 tubes ($R = 20.64$ mm) of three different wall thicknesses presented in this paper are plotted. The U_{cj} in the experiments was 2.4 km/s, at this speed $\Phi \approx 2$.

factor of 2 due to flexural wave excitation (see section 2.1) was incorporated in this static model. "Rupture" is identified with the notch breaking into a through-wall crack, and for simplification, it is assumed to be synonymous with K_I reaching K_{Ic} at the notch front.

The static model is based on the assumption that a thin-wall tube with an external axial notch under internal pressure can be treated, neglecting curvature, as a wide plate with a surface crack under far-field tension (Fig. 3). The following results of static three-dimensional finite element analysis of a wide plate with a surface crack by Newman and Raju (1981) will be used:

$$K_I = \sigma \sqrt{\frac{\pi d}{Q}} F \tag{7}$$

where

$$F = M_1 + M_2 \left(\frac{d}{h}\right)^2 + M_3 \left(\frac{d}{h}\right)^4 , \tag{8}$$

$$Q = 1 + 1.464 \left(\frac{d}{a}\right)^{1.65} , \tag{9}$$

and

$$M_1 = 1.13 - 0.09 \left(\frac{d}{a}\right) , \tag{10}$$

$$M_2 = \frac{0.89}{\left[0.2 + \left(\frac{d}{a}\right)\right]} - 0.54 , \tag{11}$$

$$M_3 = 0.5 - \frac{1.0}{\left[0.65 + \left(\frac{d}{a}\right)\right]} + 14 \left[1.0 - \left(\frac{d}{a}\right)\right]^{24} . \tag{12}$$

The K_I defined above describes the stress intensity at the deepest point of penetration for small values of d/a. The fracture condition is identified with

$$K_I = \sigma \sqrt{\frac{\pi d}{Q}} F \geq K_{Ic} . \tag{13}$$

Substituting $\sigma = \sigma_{dynamic\_max} = \Phi \Delta p R/h$ and rearranging, the rupture criterion is

$$\frac{\Phi \Delta p R \sqrt{\pi d}}{h K_{Ic}} \geq \frac{\sqrt{Q}}{F} . \tag{14}$$

The right-hand side of this equation is plotted as a surface in Fig. 25. This surface divides the parameter space into a rupture regime above the surface and non-rupture regime below the surface.

3 Experimental setup

3.1 Specimens

Two sets of experiments were performed on aluminum 6061-T6 tubes. In the first set, the notch depth (0.56 mm), notch width (0.3 mm), and tube size (0.89 mm in wall thickness, 41.28 mm in outer diameter, 0.914 m long) were kept constant for studying the fracture behavior by changing only the notch length (from 12.7 mm to 76.2 mm). The surface notch was oriented axially, located in the middle of the tube length, and cut by a CNC machine using a jeweler's slotting saw.

The second set was performed with shorter tubes (0.610 m), various flaw depth, flaw length, and wall thickness. The dimensions can be found in Table 1 in the Appendix.

Since the actual notch geometry (Fig. 2 and 3) was different from the elliptical crack geometry assumed by Newman and Raju (1981), an approximation was used to relate the model crack length, $2a$, and the 'actual' crack length, L, used in machining

$$2a = L + 2\sqrt{R_{saw}^2 - (R_{saw} - d)^2} , \tag{15}$$

where $R_{saw} = 19$ mm is the radius of the jeweler's slotting saw.

3.2 Detonation Tube Assembly

Figure 4 shows a schematic of the experimental setup for the first set of experiments with 0.914 m long specimen tubes. Figure 5 is a corresponding photograph showing the

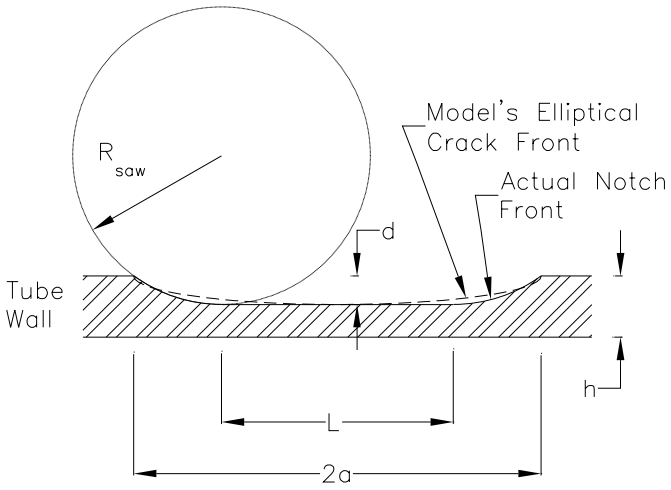

Figure 2: Flaw geometry.

assembly aligned and bolted to a plywood table. The setup consisted of two aluminum tubes connected together by a flange. The tubes were sealed at one end by a Teflon flange containing the spark plug, and the other end by a flange and a Mylar diaphragm. Inside the detonation tube, a spark first created a flame, which then transitioned to a detonation wave after being accelerated through a Shchelkin spiral. The detonation wave propagated into the thin-wall and pre-flawed specimen tube. The Mylar diaphragm burst each time so that the effects of a reflected shock wave were minimized. Pressure transducers mounted on the detonation tube measured the pressure profile and wave speeds.

For the tests with 0.610 m long tubes, an additional thick-wall extension tube with pressure transducers was connected by a flange to the aft end of the specimen tube (Fig. 6). The pressure transducers were used to study the effects of rupture on the detonation wave; these pressure data will be presented in a later study.

3.3 Instrumentation

The velocity and pressure of the detonation wave were measured by PCB piezo-electric pressure transducers. The pressure transducers were mounted 0.406 m apart in the detonation tube. The extension tube with additional pressure transducers was used only for the second set of experiments with 0.610 m long tubes.

Micro-Measurements strain gages were bonded to different locations on the external surface of the tubes to measure circumferential strain. The Trig-Tek amplifiers that amplified the signals from the Wheatstone bridges had a bandwidth of 100 kHz.

The spark and data acquisition system was triggered by a Stanford Research Systems digital pulse generator. Both the pressure traces and the strain history were digitized with Tektronix oscilloscopes at a rate of 1 MHz. The data were transferred into a computer through a LabVIEW program.

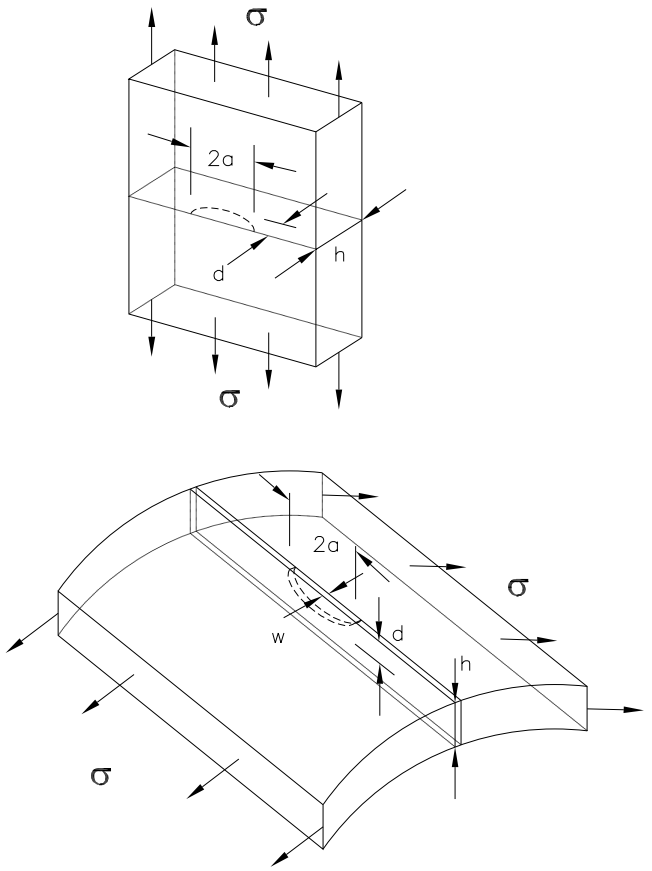

Figure 3: Flat plate model with mathematically sharp crack assumed by Newman and Raju (1981), above, compared to the tubes' actual surface notch with finite width w, below.

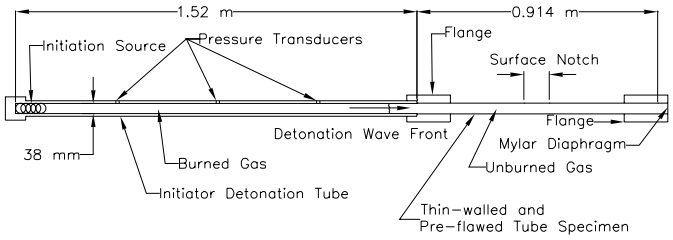

Figure 4: Tube assembly with 0.914 m long specimen.

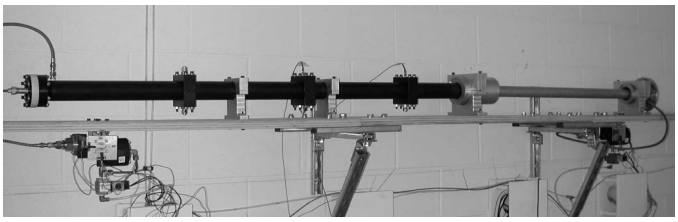

Figure 5: Tube assembly with 0.914 m long specimen.

Figure 6: Second tube assembly with 0.610 m long specimen and a 0.305 m extension tube.

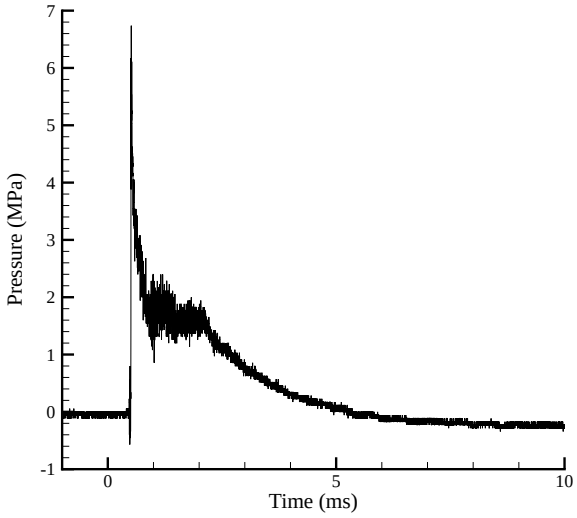

Figure 7: Typical detonation pressure trace recorded by the piezo-electric pressure transducer in the detonation tube.

4 Results and discussion

4.1 Fracture Behavior

For the first set of experiments, all parameters except one were fixed. The flaw length L was varied and different fracture behaviors were observed. The Chapman-Jouguet pressures and wave speeds were 6.2 MPa and 2390 m/s, respectively. The mixture was stoichiometric ethylene-oxygen at an initial pressure of 1.8 atm and room temperature. Figure 7 shows a typical pressure signal.

Figure 8 is a photograph of a 0.914 m long tube specimen before fracture. Figures 9 to 12 show tubes of different notch lengths after fracture. The detonation wave traveled from left to right. As the wave propagated past the surface notch, the hoop stress opened the notch into a through-wall crack. Two crack fronts then propagated–one in the forward (i.e., same direction as the detonation wave) and one in the backward direction (i.e., in the opposite direction as the detonation wave). We will refer to these two crack fronts simply as the "forward" and "backward" cracks.

Different fracture behavior was observed for the various notch lengths. For the $L = 12.7$ mm and $L = 25.4$ mm specimens (Fig. 9 and Fig. 10, respectively), both the forward and backward cracks propagated straight for some distance, then turned, ran helically around the tube, and were arrested. As the notch length increased, the cracks propagated further and created more tube fragments. Figure 11 displays a fractured 50.8 mm notch specimen. The backward crack behaved similar to those of previous specimens, but the forward crack propagated straight for only a short distance and bifurcated. The two branch cracks then ran around the tube and met on the other side, cutting the tube in two. The $L = 76.2$ mm notch specimen (Fig. 12) resulted in bifurcation of both the forward and backward cracks, cutting the tube into three pieces. The middle piece was plastically deformed until it was bent inside-out.

Another experiment on an $L = 50.8$ mm specimen was conducted to demonstrate repeatability. Figure 13 shows the resemblance of the forward bifurcated crack paths of two $L = 50.8$ mm specimens. Both specimens also exhibited similar helical and arrest behavior for the backward crack.

While bifurcated cracks tend to turn sharply (Fig. 14), helical cracks tend to turn smoothly. Cracks that bifurcated traveled straight for only a short distance (about 20 mm) after leaving the notch tip before turning sharply. Cracks that did not bifurcate traveled straight for at least 100 mm before turning smoothly.

Figure 8: Original unruptured tube.

4.2 Strain Signals

Just as the fracture behavior was studied by keeping all parameters constant except the notch length, the hoop strains near the notch were examined by keeping everything fixed

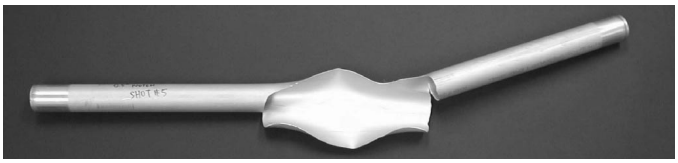

Figure 9: Ruptured tube with initial $L = 12.7$ mm notch (Shot 5).

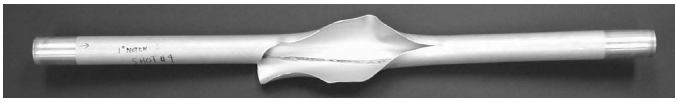

Figure 10: Ruptured tube with initial $L = 25.4$ mm notch (Shot 4).

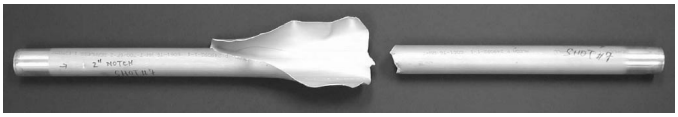

Figure 11: Ruptured tube with initial $L = 50.8$ mm notch (Shot 7).

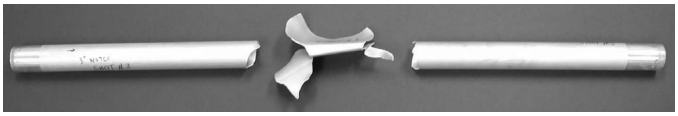

Figure 12: Ruptured tube with initial $L = 76.2$ mm notch (Shot 3).

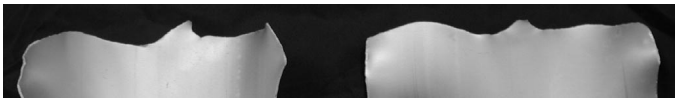

Figure 13: Resemblance of the forward bifurcated crack paths of two $L = 50.8$ mm notch specimens. The repeated experiments were run to demonstrate reproducibility (Shot 7 on the left and Shot 6 on the right).

except the pressure loading. Figure 17 shows the strains for three different specimens with the same tube and notch geometry but different detonation pressures (Shots 30, 31, and 34). As a control experiment, an identical tube with no notch and undergoing only elastic deformation was also tested (Shot 33). Time $t = 0$ corresponded to the spark used to initiate detonation. Six strain gages were placed near the notch; their locations are shown in Fig. 15. Four

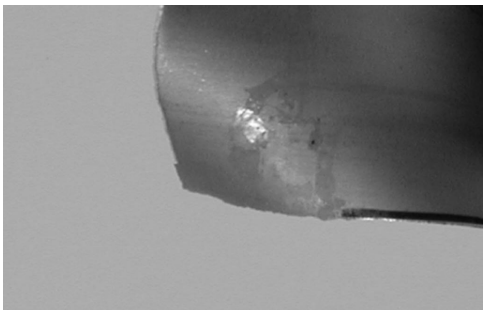

Figure 14: Sharp turn from a bifurcated crack. Darkened edge at the lower right indicates location of the initial notch.

of these were aligned with the notch, one was 90° from the notch, and one was 180°. Figures 19 to 23 are photographs of tubes 33, 31, 30, 34, and 24, respectively, after each shot (detonation wave direction is from left to right). Figure 24 shows a schematic of crack propagation direction for Shots 34 and 24. The strain rates ranged from 10^2 s^{-1} to 10^3 s^{-1}.

Shot 33 shows typical elastic strains of flexural waves excited by detonation waves that travel above v_{c0} but below v_{c1}. While the reader is referred to Beltman and Shepherd (2002) for a more detailed discussion, several points are worth mentioning here. First, the strain front coincides with the detonation wave front. Second, the frequencies of the strains correspond closely to the Tang (1965) model's theoretical steady-state frequency, which is 50 kHz for this tube. Third, the measured Φ here is about 1.5, and thus, our assumed value of 2 for the fracture threshold model is apparently too high. Fourth, since the flexural waves were dispersive and the detonation wave was traveling above v_{c0}, precursor waves at frequencies over 1 MHz would travel ahead of the strain signals seen here. The reasons that they are invisible are that 1) they are of small amplitude compared to the main signal, and 2) the amplifiers, having a bandwidth of 100 kHz, attenuated the high frequency precursors. Fifth, the differences between individual gage signals despite their close proximity may be caused by non-axisymmetric boundary conditions due to the imperfect alignment of the specimen tube with the flanges and multiple reflections of different kinds of waves from the tube ends.

Comparison between Shots 31 (notched tube with no rupture) and 33 (no notch and no rupture) reveals that the presence of the notch reverses the sign of the hoop strains (gages 2 and 3) near the notch. This is expected because as the notch edges bulged under internal pressure, the local curvature of the shell changed and the local strain became compressive. Figure 16 shows an illustration. This effect was not experienced by gages 1, 4, 5, and 6 as they were

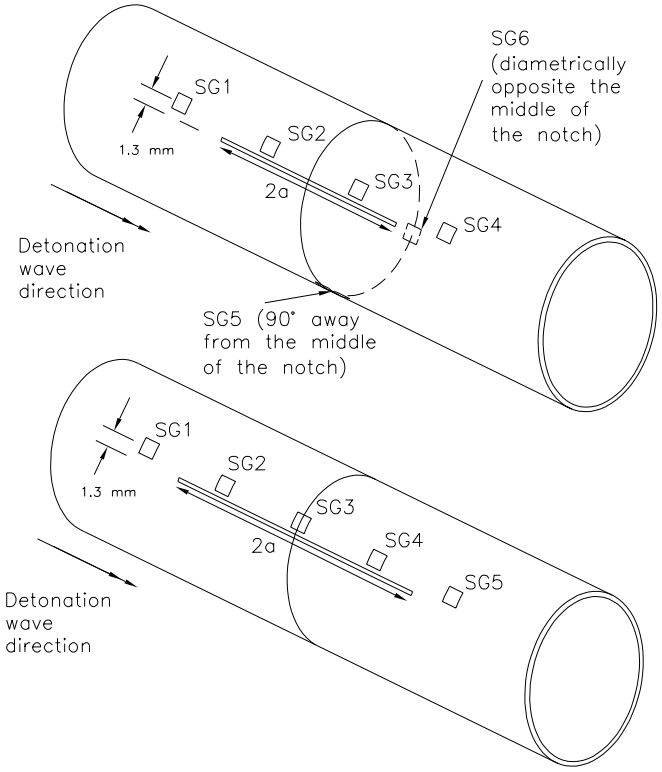

Figure 15: Strain gage locations for Shots 30, 31, and 34 (above) and Shot 24 (below). Distance between gages was 15.2 mm for gages 1 through 4 for Shots 30, 31, and 34. Distance between gages was 25.4 mm for Shot 24. The strain gage locations for Shot 33 follow that of 30, 31, and 34. Gage length was 0.81 mm and gage width was 1.52 mm. Drawing is not to scale.

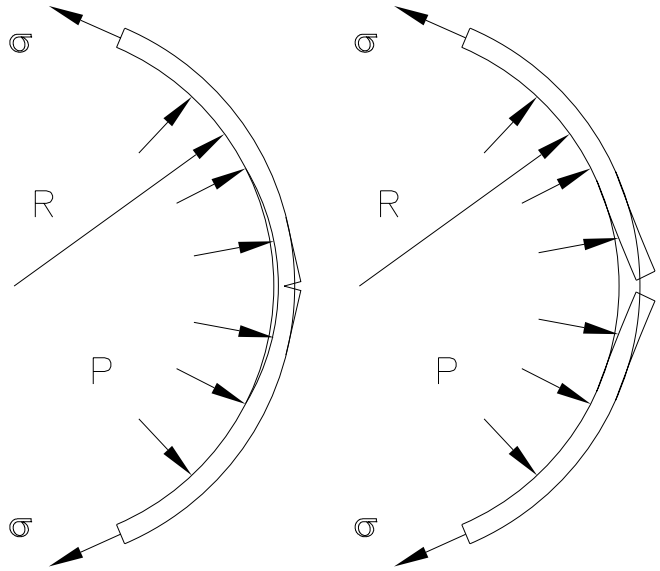

Figure 16: Bulging of the notched and cracked areas caused the local shell curvature to change and thus, gave rise to local compressive strains recorded by strain gages.

farther away from the notch.

In Shot 30, a higher pressure was used on a notched tube, which ruptured with the crack confined inside the notch. An abrupt change from tensile to compressive strains for gages 1 and 4 and the sudden increase in compression for gages 2 and 3 suggest that crack initiation occurred at about 4.2 ms, or 0.2 ms after the arrival of the detonation wave front. The change in sign for gages 1 and 4 is due to increased bulging after the loss of material continuity in the notch.

Shot 34 was an example of catastrophic structural failure in which cracks propagated both in the forward (following the detonation wave) and backward directions. The two cracks propagated in a helical fashion. Because of the emerging detonation products from the crack, some of the gages did not survive long enough to provide meaningful data. Gages 2 and 3 were put into compression, while gages 1 and 4 were in tension for about 0.1 ms and then abruptly went into compression when the cracks propagated past the gage location, causing the local shell surface to bulge. Note that strain gage 4 reverted from tension to compression slightly earlier than gage 1, suggesting that the forward crack was propagating faster than the backward crack.

Figure 18 shows strain signals for a specimen whose forward crack bifurcated and the backward crack ran helically. The five strain gages are all aligned with the notch (Fig. 15) and were located differently from those of Shots 30, 31, 33, and 34. The forward crack ran straight for a short distance, passing strain gage 1 before branching into two secondary cracks. The gage recorded tension for a brief period, but then transitioned to compression as did gage 1 in Shot 34. Strain gages 2 thru 4 in Shot 24 behaved similarly to gages 2 and 3 in Shot 34, while gage 5 in Shot 24 behaved similarly to gage 4 in Shot 34.

In all the five cases just discussed, the detonation wave travelled at 2.4 km/s. This means that the detonation wave front took 0.1 ms to travel from the strain gages to the end of the specimen tube. The pressure traces in the initiator tube give the approximate duration from the detonation wave front's arrival at the pressure transducer to completion of venting of the detonation products (i.e., coming to atmospheric pressure). It was found that for all the five cases above, this tube venting time was at least 5 ms.

Abrupt strain jumps at later times such as gage 2 at 4.7 ms for Shot 34, gage 1 at 5.1 ms, and gage 2 at 4.8 ms for Shot 24 were probably due to the flaps of tube material (created by fracture) impacting the support structure.

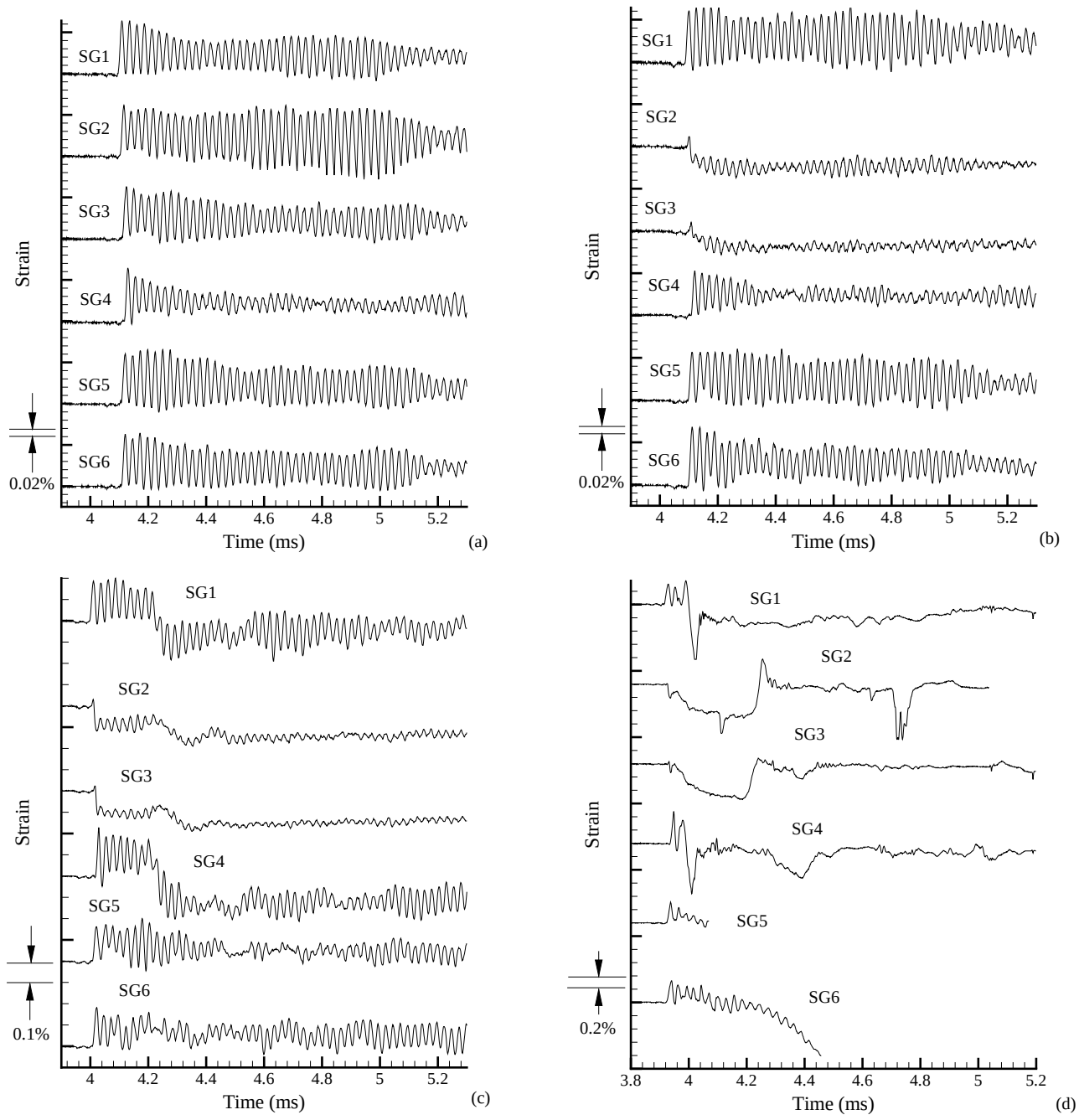

Figure 17: Hoop strain of four specimens with the same wall thickness and tube length. The flaw sizes were also the same, except Shot 33, which had no notch. All strain traces start at zero strain. (a) tube with no notch and no rupture (Shot 33). (b) notched tube with no rupture (Shot 31). (c) notched tube with rupture confined within the notch (Shot 30). (d) notched and ruptured tube with forward and backward helical cracks (Shot 34).

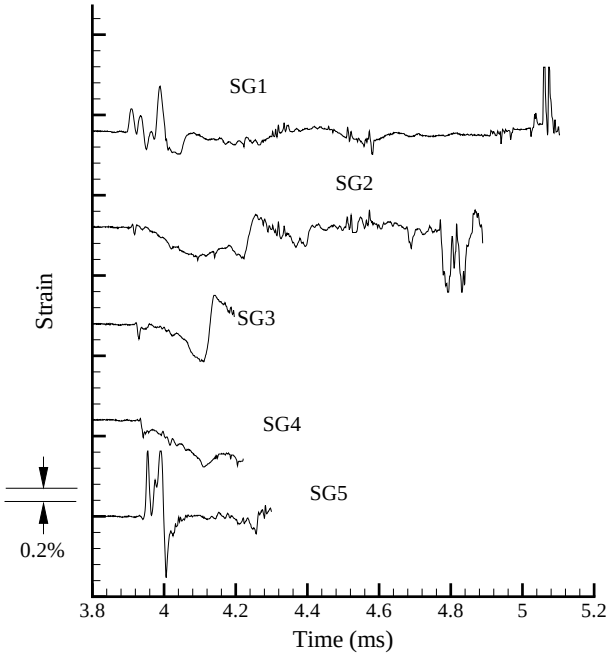

Figure 18: Notched and ruptured tube with forward bifurcated cracks and backward helical cracks (Shot 24).

Figure 19: Tube with no notch and no rupture (Shot 33).

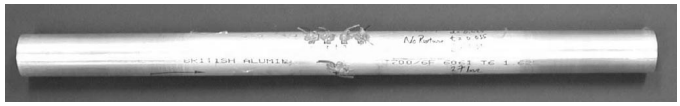

Figure 20: Notched tube with no rupture (Shot 31).

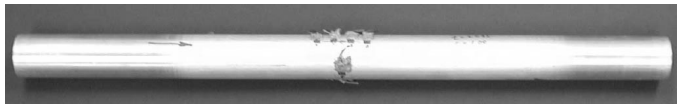

Figure 21: Notched tube with rupture confined within the notch (Shot 30).

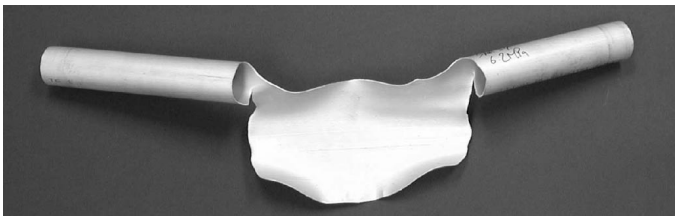

Figure 22: Notched and ruptured tube with forward and backward helical cracks (Shot 34).

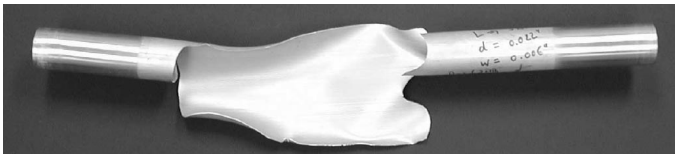

Figure 23: Notched and ruptured tube with forward bifurcated cracks and backward helical crack (Shot 24).

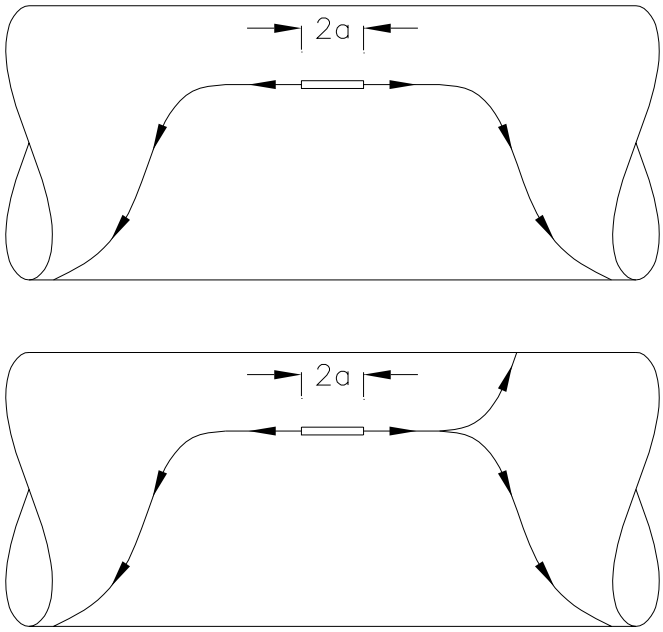

Figure 24: Schematic of crack propagation direction. Above: Shot 34. Below: Shot 24. Detonation wave ran from left to right. Drawing is not to scale.

4.3 Fracture Threshold

The second set of experiments used shorter tubes (0.610 m) and the parameters being varied included flaw depth, flaw length, wall thickness, and pressure. Experiments on twenty-five Al6061-T6 tubes of this length were performed (see Appendix for loading and geometry). The results are plotted on Fig. 25 using the left-hand side of Eq. 14. The right-hand side of Eq. 14 is the theoretical threshold surface, plotted on the same figure for comparison.

The agreement between theory and experiment is better than expected for a model based on static relations. Experiments have not yet been performed on higher values of d/h because a shallower initial flaw requires higher detonation pressure to rupture. The current facility is being modified to accommodate detonations at higher pressures.

4.4 Fractographs

Light microscope pictures of fracture surfaces were taken and some of these are shown in Fig. 26. Detonation wave direction is from left to right. The magnification was 30X, using a Leica GZ4 light microscope. The natural scale in these photos is the wall thickness of the tubes, which is 0.89 mm. The roughness of the surfaces indicate ductile fracture.

Conclusion

The current model, while being able to identify the trend for fracture threshold, needs much improvement. A fully dynamic numerical model must be developed in the future to account for bending, shear, inertia, and plasticity. The strain signals obtained can be used as a reference for the future numerical simulations. Moreover, the specimens had blunt notches that are dissimilar from the mathematically sharp crack which the static model assumes. To ensure better agreement between experiment and analysis, one must overcome the challenge of either initiating a sharp crack (and knowing how deep it has penetrated) in the tube before each experiment, or developing a numerical method that accounts for the bluntness of the notch. Finally, of important concern is the multi-cycle nature of the stresses that is obvious from the strain signals. Numerical analysis that attempts to predict whether or not the initial crack has propagated through the wall thickness must account for not only the first cycle, but also multiple cycles of stresses, and how, during that period, the size of the dynamic stress intensity field evolves as a function of time.

Acknowledgments

The authors would like to thank Professor W. G. Knauss and Professor G. Ravichandran for their helpful discussions. This research was sponsored in part through the Office of Naval Research (ONR) contract N00014-99-1-0744. Their support is gratefully acknowledged.

References

Beltman, W., E. Burcsu, J. Shepherd, and L. Zuhal, 1999. The structural response of tubes to internal shock loading. *Journal of Pressure Vessel Technology 121*, 315–322.

Beltman, W. and J. Shepherd, 2002. Linear elastic response of tubes to internal detonation loading. *To appear in Journal of Sound and Vibration*.

de Malherbe, M., R. Wing, A. Laderman, and A. Oppenheim, 1966. Response of a cylindrical shell to internal blast loading. *Journal of Mechanical Engineering Science 8*(1), 91–98.

Folias, E. S., 1965. A finite crack in a pressurized cylindrical shell. *International Journal of Fracture Mechanics 1*, 104–113.

Kiefner, J. F., W. A. Maxey, R. J. Eiber, and A. R. Duffy, 1973. Failure stress levels of flaws in pressurized cylinders. In *ASTM STP 536, Progress in Flaw Growth and Fracture Toughness Testing, Proceedings of the 1972 National Symposium on Fracture Mechanics*.

Maxey, W. A., J. F. Kiefner, R. J. Eiber, and A. R. Duffy, 1971. Ductile fracture initiation, propagation, and arrest in cylindrical vessels. In *ASTM STP 514, Fracture Toughness, Proceedings of the 1971 National Symposium on Fracture Mechanics PART II*.

Newman, Jr., J. and I. S. Raju, 1981. An empirical stress-intensity factor equation for the surface crack. *Engineering Fracture Mechanics 15*(1-2), 185–192.

Reismann, H., 1965. Response of a pre-stressed cylindrical shell to moving pressure load. In S. Ostrach and R. Scanlon (Eds.), *Eighth Midwest Mechanics Conference*, pp. 349–363. Pergamon Press.

Simkins, T., 1987, July. Resonance of flexural waves in gun tubes. Technical Report ARCCB–TR–87008, US Army Armament Research, Development and Engineering Center, Watervliet, N.Y. 12189–4050.

Tang, S., 1965, October. Dynamic response of a tube under moving pressure. In *Proceedings of the American Society of Civil Engineers*, Volume 5, pp. 97–122. Engineering Mechanics Division.

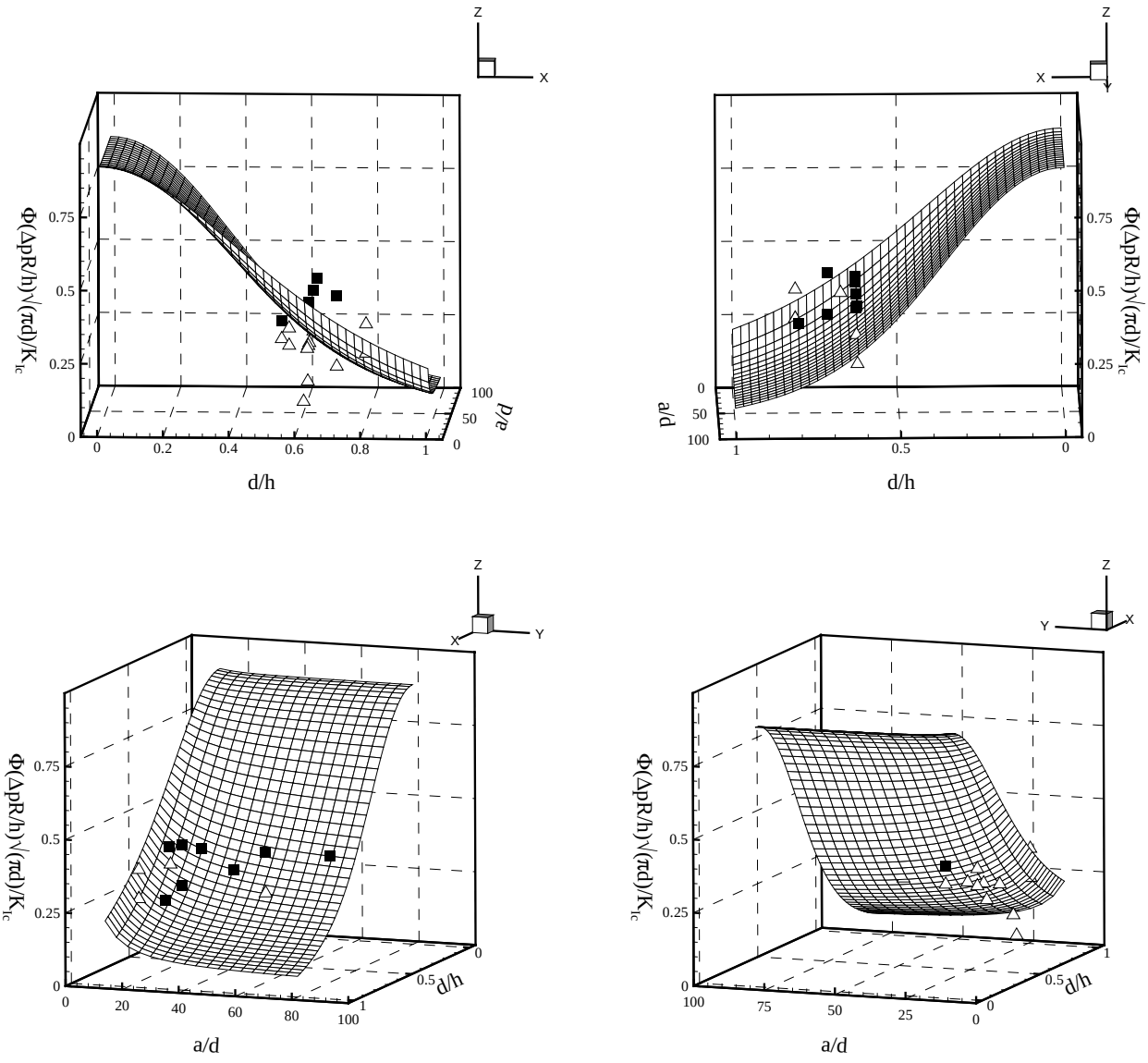

Figure 25: Different perspective views of the fracture threshold. The surface divides the space into theoretical rupture (above) and no rupture regimes (below) according to Eq. 14. Experimental data are presented as filled squares for ruptured tubes and open triangles for intact tubes.

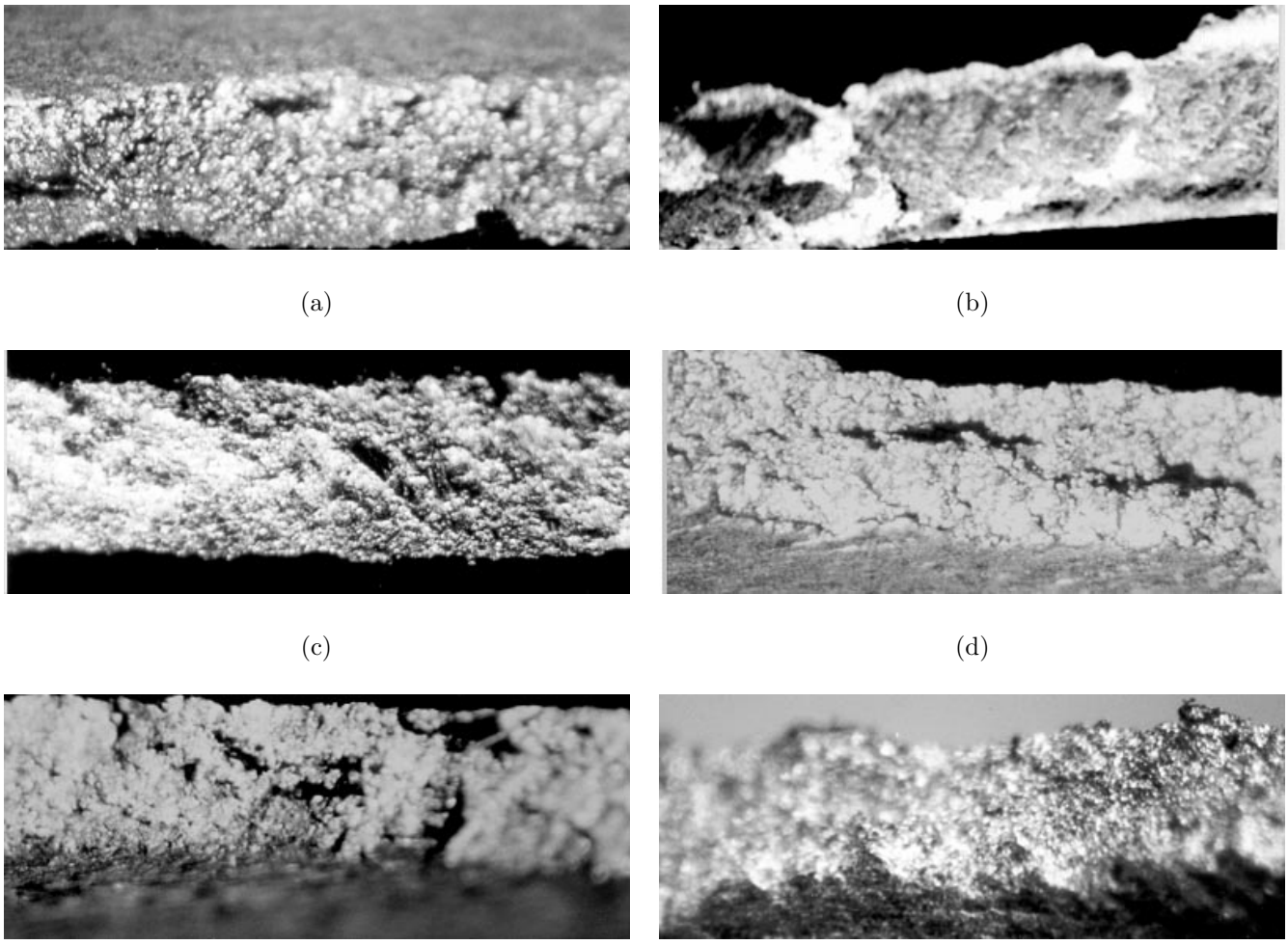

(a) (b)

(c) (d)

(e) (f)

Figure 26: Fractographs. (a) backward crack surface near notch tip before running helically (Shot 24). (b) forward crack surface near notch tip before bifurcation (Shot 24). (c) forward crack surface near notch tip before running helically (Shot 29). (d) backward crack surface far from notch tip before running helically (Shot 34). (e) forward crack surface far from notch tip before running helically (Shot 34). (f) forward crack surface near notch tip before running helically (Shot 34).

Appendix

Flaw					*Tube (R = 20.64 mm)*		*Detonation Wave*		*Result*
Shot	d (mm)	w (mm)	L (mm)	$2a$ (mm)	l (m)	h (mm)	U_{cj} (m/s)	P_{cj} (MPa)	*Ruptured?*
3	0.56	0.3	76.2	85.4	0.914	0.89	2390	6.2	y
4	0.56	0.3	25.4	34.6	0.914	0.89	2390	6.2	y
5	0.56	0.3	12.7	21.9	0.914	0.89	2390	6.2	y
6	0.56	0.3	50.8	60.0	0.914	0.89	2390	6.2	y
7	0.56	0.3	50.8	60.0	0.914	0.89	2390	6.2	y
9	0.91	0.2	12.7	24.4	0.610	1.5	2351	2.0	n
10	0.79	0.2	12.7	23.5	0.610	1.2	2371	3.0	n
11	0.56	0.2	12.7	21.9	0.610	0.89	2385	4.1	n
12	0.56	0.2	19.1	28.2	0.610	0.89	2385	4.1	n
13	0.56	0.2	25.4	34.6	0.610	0.89	2385	4.1	n
14	0.56	0.2	38.1	47.3	0.610	0.89	2396	5.2	y
15	0.56	0.2	50.8	60.0	0.610	0.89	2385	4.1	n
16	0.48	0.2	25.4	33.9	0.610	0.89	2399	5.5	y
17	0.48	0.2	25.4	33.9	0.610	0.89	2389	4.5	n
18	1.2	0.2	25.4	38.7	0.610	1.5	2389	4.5	n
19	1.2	0.2	25.4	38.7	0.610	1.5	2389	4.5	n
24	0.56	0.2	76.2	85.4	0.610	0.89	2390	6.2	y
25	0.71	0.2	25.4	35.7	0.610	1.2	2395	5.1	n
26	0.71	0.2	25.4	35.7	0.610	1.2	2390	6.2	n
28	0.84	0.2	25.4	36.6	0.610	1.2	2390	6.2	n
29	0.71	0.2	25.4	35.7	0.610	0.89	2377	3.5	y
30	0.64	0.2	25.4	35.2	0.610	0.89	2386	4.2	y
31	0.64	0.2	25.4	35.2	0.610	0.89	2366	2.7	n
32	1.2	0.2	25.4	38.7	0.610	1.5	2390	6.2	n
33	–	–	–	–	0.610	0.89	2366	2.7	n
34	0.64	0.2	25.4	35.2	0.610	0.89	2390	6.2	y

Table 1: Test Matrix

K_{Ic} (Static)	30 MPa$\sqrt{\text{m}}$
ρ	2780 kg/m^3
E	69 GPa
ν	0.33

Table 2: Aluminum 6061-T6 properties